




Article

Impact of Aperture, Depth, and Acoustic Clutter on the Performance of Coherent Multi-Transducer Ultrasound Imaging

Laura Peralta ^{1,*}, Alessandro Ramalli ², Michael Reinwald ¹, Robert J. Eckersley ¹
and Joseph V. Hajnal ¹

¹ Department of Biomedical Engineering, School of Biomedical Engineering & Imaging Sciences, King's College London, London SE1 7EH, UK; mchlrrnwd@gmail.com (M.R.); robert.eckersley@kcl.ac.uk (R.J.E.); jo.hajnal@kcl.ac.uk (J.V.H.)

² Department of Information Engineering, University of Florence, 50139 Florence, Italy; alessandro.ramalli@unifi.it

* Correspondence: laura.peralta_pereira@kcl.ac.uk

Received: 16 September 2020; Accepted: 22 October 2020; Published: 29 October 2020



Abstract: Transducers with a larger aperture size are desirable in ultrasound imaging to improve resolution and image quality. A coherent multi-transducer ultrasound imaging system (CoMTUS) enables an extended effective aperture through the coherent combination of multiple transducers. In this study, the discontinuous extended aperture created by CoMTUS and its performance for deep imaging and through layered media are investigated by both simulations and experiments. Typical image quality metrics—resolution, contrast and contrast-to-noise ratio—are evaluated and compared with a standard single probe imaging system. Results suggest that the image performance of CoMTUS depends on the relative spatial location of the arrays. The resulting effective aperture significantly improves resolution, while the separation between the arrays may degrade contrast. For a limited gap in the effective aperture (less than a few centimetres), CoMTUS provides benefits to image quality compared to the standard single probe imaging system. Overall, CoMTUS shows higher sensitivity and reduced loss of resolution with imaging depth. In general, CoMTUS imaging performance was unaffected when imaging through a layered medium with different speed of sound values and resolution improved up to 80% at large imaging depths.

Keywords: multi-probe; large aperture; ultrasound imaging; acoustic clutter

1. Introduction

Limited resolution and a restricted field of view (FOV) are two of the main challenges in ultrasound (US) imaging that, in principle, are fundamentally limited by the extent of the transmitting and receiving apertures. The image lateral resolution of ultrasonography is diffraction limited and mostly depends on the wavelength of the transmission wave, the imaging depth and the aperture size (measured by the F-number) [1]. However, since high frequency acoustic waves are easily absorbed and attenuated by tissues, the use of low frequencies is the only choice when the imaging region is located in deep areas in the body. Consequently, a large aperture size is desired to decrease the F-number and improve resolution and FOV.

Nevertheless, it is not clear that a large aperture will overcome the expected resolution loss through depth in the presence of acoustically heterogeneous tissues [2]. Inhomogeneities and tissue layers with different acoustic properties cause phase errors restricting the improvements provided by large arrays [3]. Transabdominal US imaging is particularly difficult in obese patients because of the increased imaging depth with longer attenuation paths and the presence of clutter associated with

boundaries between regions with dissimilar properties [4,5]. Difficult abdominal imaging tasks require an array design that provides sufficient penetration for the chosen target depth, adequate resolution for the diagnostic task and tolerance to acoustic clutter effects that degrade the backscattered echo signals. The need for the development of large arrays for high resolution abdominal diagnostic imaging has been already suggested by previous studies, where a large array was synthesized through a synthetic aperture method by combining the received data from multiple positions of the same probe [6,7]. However, in such a method, the final coherent aperture is limited by the long acquisition times, and the image quality is very sensitive to calibration errors and noise in the tracking system.

Despite a large aperture being desirable, the practical aperture size is often limited by the complexity and cost of scanners and probes based on large channel count arrays and the low flexibility for some applications. Using collections of conventional existing arrays to extend the aperture may be a way to approach this problem. Indeed, the use of multiple conventionally sized arrays to create a large aperture instead of using a single big array may be more flexible for diverse applications, e.g., for intercostal imaging, where the acoustic windows are narrow. In practice, multiple probes can be manipulated using a single and potentially adjustable holder that allows the operator to hold multiple probes with only one hand while keeping them directed to the same region of interest [8]. In that first study, images were compounded incoherently, which, as is well known, allows the exploitation of a diversity of points of views, but does not directly achieve the gains in resolution and sensitivity that could be realised if the multiple probes were fully and coherently combined into a one large effective aperture. Hence, coherent multi-transducer ultrasound (CoMTUS) imaging, which combines all radio frequency (RF) data received by multiple synchronized transducers that take turns transmitting plane waves (PWs) into a common FOV, was introduced by our group to further improve ultrasound (US) imaging performance [9,10]. CoMTUS yields images with an extended FOV and higher resolution, while preserving, at the same time, a reasonably high frame rate. It provides a first step toward large aperture imaging using independently placed transducers to form discontinuous extended apertures. In contrast to other proposed techniques [6,7], CoMTUS achieves the subwavelength localization accuracy required to combine information from multiple transducer poses, without the use of any external tracking device by optimizing the beamforming parameters [10]. These optimal beamforming parameters, which include the transducers' location and the average speed of sound (SOS), are deduced by maximizing the coherence of the received RF data resulting from different targeted scatterers in the medium by cross-correlation.

One key feature of CoMTUS is the resulting discontinuous aperture. Preliminary studies showed that an improved spatial resolution comes with a loss in image contrast [11,12]. Nevertheless, how much the aperture's discontinuities, dictated by the spatial separation of the multiple transducers, affect the global performance of the method is still unclear. Moreover, so far, CoMTUS has been validated only in constant SOS media, which is known not to be representative of human tissues. Therefore, to prepare for future in vivo applications, the purpose of this study is to further investigate the performance of CoMTUS to better assess its potential benefits and describe its implications for imaging. First, the impact of the effective aperture size, the separation between the arrays, the imaging depth and the presence of acoustic clutter will be assessed in a parametric study. Then, the behaviour of CoMTUS, particularly of the optimized beamforming stage, will be shown when assuming different and spatially varying speeds of sound, i.e., by assuming path dependent SOS due to variable thickness layers of tissue with different acoustic properties.

The paper is organized as follows: Section 2 briefly recalls the theory of CoMTUS, then Section 3 presents the Materials and Methods, with simulations described in Section 3.1 and the corresponding experimental methods in Section 3.2. To establish a description of the CoMTUS discontinuous aperture, different effective aperture sizes and the corresponding images are simulated. The method is then evaluated at large imaging depths. Then, the CoMTUS method, initially validated in homogeneous media, is extended to a model of layered tissue with different speeds of sound. Results are presented in Section 4 and discussed in Section 5. Finally, the study is concluded in Section 6.

2. Theory: Coherent Multi-Transducer Ultrasound Imaging

A CoMTUS system consists of N synchronized US arrays that take turns transmitting PWs into a common FOV. Only one individual array transmits at each time while all N arrays simultaneously receive. The subwavelength localization accuracy required to coherently combine RF data from multiple probes is achieved without the use of any external tracking device. The method is briefly summarized in this section, but more details can be found in [9,10,13].

In this study, we consider a CoMTUS system formed by $N = 2$ identical linear arrays that lie in the same elevational plane ($y = 0$) and are angled relative to each other so as to share part of the FOV, as shown in Figure 1. In such a configuration, the following nomenclature is used. For a sequence in which array i transmits and array j receives, the RF data received on channel h of array j at time t are named $T_i R_j(h, t)$. The resulting image and all transducer coordinates are defined in a global coordinate system arbitrarily located in space (\hat{x}_0, \hat{z}_0) . For a given linear array i , a local coordinate system (\hat{x}_i, \hat{z}_i) is defined at the centre of the array surface with the \hat{z} direction orthogonal to the transducer surface and directed away from array i . The position and orientation of array i are then characterized in the global coordinate system with three parameters that define a translation vector \mathbf{r}_i and a rotation angle θ_i [14].

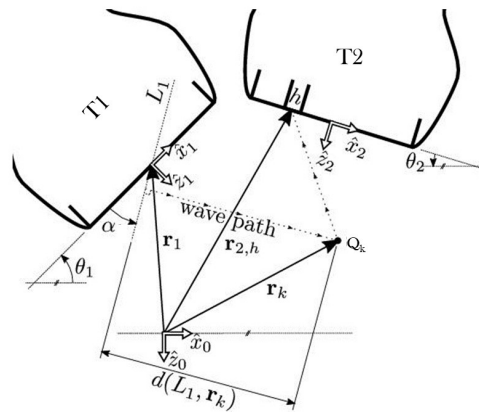


Figure 1. Coherent multi-transducer ultrasound (CoMTUS) beamforming scheme. The global and local coordinates of the arrays are shown. In this example, array T1 transmits a plane wave (PW) at angle α , and array T2 receives the resulting echoes backscattered from the scatter Q_k .

Standard delay and sum beamforming for PW imaging [15] can be extended to the present multi-transducer setup taking into account the full path length between the transmit array and the receive elements. Considering that array i transmits a PW at certain angle α , the image point to be beamformed located at Q_k and described by the vector \mathbf{r}_k can be computed from the echoes received at transducer j as:

$$s_{i,j}(Q_k; \alpha) = \sum_{h=1}^H T_i R_j \left(h, t_{i,j,h}(Q_k; \alpha) \right) = \sum_{h=1}^H T_i R_j \left(h, \frac{D_{i,j,h}(Q_k; \alpha)}{c} \right) \quad (1)$$

where H is the total number of elements in the array, c is the average SOS of the propagation medium and $t_{i,j,h}(Q_k; \alpha)$ is the time-of-flight of a PW at angle α transmitted by array i , backscattered by the point Q_k and received by the element h of array j . The total distance $D_{i,j,h}(Q_k; \alpha)$ travelled by the wave is defined by,

$$D_{i,j,h}(Q_k; \alpha) = d(L_i(\alpha), \mathbf{r}_k) + \|\mathbf{r}_{j,h} - \mathbf{r}_k\| \quad (2)$$

where $d(\mathbf{r}_k, L_i(\alpha))$ is the distance from \mathbf{r}_k to the line $L_i(\alpha)$ that defines the transmitted PW and $\|\mathbf{r}_{j,h} - \mathbf{r}_k\|$ is the Euclidean distance between \mathbf{r}_k and the receive element h of array j . These distances are represented in Figure 1.

Finally, the total beamformed image $S(Q_k; \alpha)$ can be obtained by coherently adding the individually beamformed images acquired in a sequence in which both probes transmit:

$$S(Q_k; \alpha) = s_{1,1}(Q_k; \alpha) + s_{1,2}(Q_k; \alpha) + s_{2,1}(Q_k; \alpha) + s_{2,2}(Q_k; \alpha) \quad (3)$$

In the same way, several PWs transmitted at different angles, $a = 1, \dots, A$, may be coherently combined to generate an image,

$$S(Q_k; A) = \sum_{i=1}^N \sum_{j=1}^N \sum_{a=1}^A s_{i,j}(Q_k; \alpha_a^i) \quad (4)$$

The optimum beamforming parameters that determine Equation (1) ($\mathcal{P} = \{c, \theta_1, \mathbf{r}_1, \theta_2, \mathbf{r}_2\}$), not a priori accurately known, are calculated by maximizing the cross-correlation of backscattered signals from common point-like targets acquired by individual receive elements, by using gradient based optimization methods,

$$\bar{\mathcal{P}} = \arg \max_{\mathcal{P}} \chi(\mathcal{P}) \quad (5)$$

where the cost function $\chi(\mathcal{P})$ is defined as follows,

$$\chi(\mathcal{P}) = \sum_k^K \sum_h^H \{ \text{NCC}(T_1 R_1(h, t_{1,1,h}(Q_k; \mathcal{P})), T_2 R_1(h, t_{2,1,h}(Q_k; \mathcal{P}))) W_{1,1} W_{2,1} + \text{NCC}(T_1 R_2(h, t_{1,2,h}(Q_k; \mathcal{P})), T_2 R_2(h, t_{2,2,h}(Q_k; \mathcal{P}))) W_{1,2} W_{2,2} \} \quad (6)$$

NCC is the normalized cross-correlation, and $W_{i,j}$ is a weighting factor defined as,

$$W_{i,j}(\mathcal{P}) = \frac{1}{2} + \frac{1}{2H} \sum_{h_b \neq h}^H \text{NCC}(T_i R_j(h; t_{i,j,h}(\mathcal{P})), T_i R_j(h_b; t_{i,j,h}(\mathcal{P}))) \quad (7)$$

A minimum of two points is needed to solve this trilateration problem in 2D [16]. Although, since the approach relies on a measure of coherence, which may well be more tolerant, previous results suggest that the method may work when there are identifiable prominent local features [10]. On the other hand, isolated point scatterers can be artificially generated by other techniques, for instance by inclusion of microbubble contrast agents [17]. Preliminary results show the potential of microbubbles to optimize the beamforming parameters in CoMTUS, which could be implemented in vivo wherever the FOV contains vasculature [18].

3. Materials and Methods

3.1. Simulations

The k-Wave Matlab toolbox was used to simulate 2D non-linear wave propagation through an inhomogeneous dispersive medium [19,20]. A CoMTUS system formed by two identical linear arrays, similar to the ones experimentally available, was simulated as follows. Each of the arrays had a central frequency of 3 MHz and 144 active elements in both transmit and receive, with an element pitch of 240 μm and kerf of 40 μm . For PWs, the modelled transducer had an axial focus of infinity with all 144 elements firing simultaneously. A simulation was performed for each transmit event, i.e., each PW at a certain angle. In total, seven transmit simulations per linear array were performed to produce a PW dataset, which covered a total sector angle of 30° (from -15° to 15° , 5° step). In the case of CoMTUS, this results in 14 transmit events in total (seven PWs per array). This PW sequence was chosen to match in resolution a focused system with an F-number of 1.9, decimating the required number of angles by a factor of six to optimize the simulation time without affecting resolution [21]. The computational grid was set following convergence testing from a previous study [22]. The spatial grid was fixed at

40 μm (six grid points per wavelength) with a time step of 1.3 ns. The power law exponent to model frequency-dependent attenuation was set to 1.5 [23]. Received signals were downsampled at 30.8 MHz. Channel noise was introduced to the RF simulated data as white Gaussian noise. The signal-to-noise ratio (SNR) for all simulated data was set to 35 dB at a 50 mm imaging depth.

The US pulses were propagated through heterogeneous scattering media using tissue maps defined by the SOS, density, attenuation and nonlinearity (see Table 1). A medium defined only with the properties of general soft tissue was used as the control case. To model the scattering properties observed in vivo, scatterers with a size smaller than the wavelength of the transmitted signal were added to the tissue maps. In order to fully develop speckle [24], a total of 15 scatterers of 40 μm in diameter, with random spatial position and amplitude (defined by a 5% difference in SOS and density from the surrounding medium), were added per resolution cell, the size of which was assumed to be 0.5 mm^2 . Three point-like targets and an anechoic lesion were included in the media to allow the measurement of the basis metrics for comparing the imaging quality for different scenarios. A circular anechoic lesion of 12 mm in diameter located at the centre of the aperture of the common FOV was modelled as a region without scatterers. The point-like targets were simulated as circles of 0.2 mm in diameter with a 25% difference in SOS and density with the surrounding tissue to generate appreciable reflection. The same realization of scatterers was superimposed on all maps and through the different simulations to keep the speckle pattern in the CoMTUS system, so any changes in the quality imaging metrics were due to changes in the overlying tissues, the imaging depth and the acoustical field.

The k-Wave Matlab toolbox uses a Fourier co-location method to compute spatial derivatives and numerically solve the governing model equations, which requires discretisation of the simulation domain into an orthogonal grid. Consequently, continuously defined acoustic sources and media need to be sampled on this computational grid, introducing staircasing errors when sources do not exactly align with the simulation grid [25,26]. To minimize these staircasing errors, the transmit array was always aligned to the computational grid, i.e., simulations were performed in the local coordinate system of the transmit array. This implies that to simulate a sequence in which the array T2 transmits, the propagation medium, including the sub-resolution scatterers, was converted into the local coordinate system of probe T2 using the same transformation matrix that defines the relative position of both arrays in space. A sample tissue map with the transducers, targets and anechoic lesion locations, represented in both local coordinate systems, is shown in Figure 2.

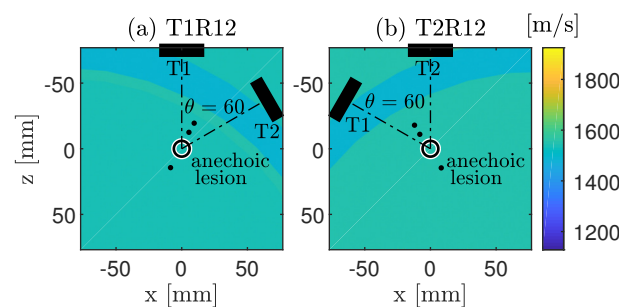


Figure 2. Example of the speed of sound map of a propagation medium with a muscle layer of 8 mm and a fat layer of 25 mm in thickness. Locations of US probes, point-like targets and anechoic lesion are shown. (a) Medium expressed in the local coordinate system of the array T1 and used to simulate the RF data T1R12, i.e., when the array T1 transmits. (b) Medium expressed in the local coordinate system of the array T2 and used to simulate the RF data T2R12, i.e., when the array T2 transmits. In this example, the angle between the probes that defines their position in space is 60° and the corresponding imaging depth 75 mm.

Table 1. Tissue map properties.

Tissue Type	SOS (m/s)	Density (kg/m ³)	Attenuation (dB/MHz/cm)	Nonlinearity B/A
Soft tissue	1540	1000	0.75	6
Fat	1478	950	0.63	10
Muscle	1547	1050	0.15	7.4

3.1.1. CoMTUS Discontinuous Effective Aperture

Previous results showed that the discontinuous effective aperture obtained by CoMTUS determines the quality of the resulting image [9,11]. To investigate the effects of the discontinuous aperture, determined by the relative location of the CoMTUS arrays in space, different CoMTUS systems with the arrays located at different spatial locations were modelled. Simulations were performed in the same control medium, where only soft tissue material was considered. To modify the relative location of the probes while keeping the imaging depth (fixed at 75 mm), the angle between the arrays was changed. The array T1 was always positioned at the centre of the x -axis of the simulation grid, while the array T2 was rotated around the centre of the propagation medium. Then, different cases of CoMTUS with two arrays located at different angles (30° , 45° , 60° and 75°) were simulated. Figure 3a shows a schematic representation of the probes in space, where the different spatial parameters (angle between probes, θ , and gap, Gap , in the resulting effective aperture, Ef) are labelled. Note that, at larger angles, both the effective aperture of the system defined by both probes and the gap between them increase. The relationships between probe position and the resulting effective aperture and gap are shown in Figure 3b.

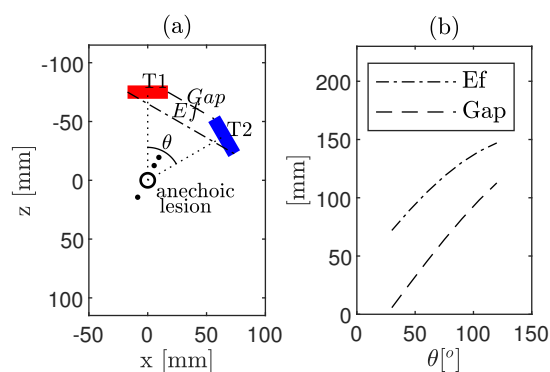


Figure 3. (a) Schematic representation of the spatial location of the two linear arrays, T1 (red) and T2 (blue), three point-like targets and the anechoic lesion in the local coordinate system of T1. Different geometrical parameters are shown: angle between probes (θ) and the gap (Gap) in the resulting effective aperture (Ef). (b) Associations between θ , Gap and the resulting Ef .

3.1.2. CoMTUS Imaging Depth

The dependence of CoMTUS performance on imaging depth was investigated by changing the local orientation of the arrays and using the same control propagation medium (only soft tissue). For a given effective aperture (fixed gap ~ 45.3 mm), each probe was rotated around its centre by the same angle, but in the opposite direction. In that way, a certain given rotation, for example negative in T1 and positive in T2, will result in a deeper common FOV, and the opposite for the counter rotation. Figure 4 shows the imaging depth dependence on the transducer orientation (defined by the position of the common FOV of both arrays). Using this scheme, four different imaging depths were simulated: 57.5 mm, 75 mm, 108 mm and 132 mm.

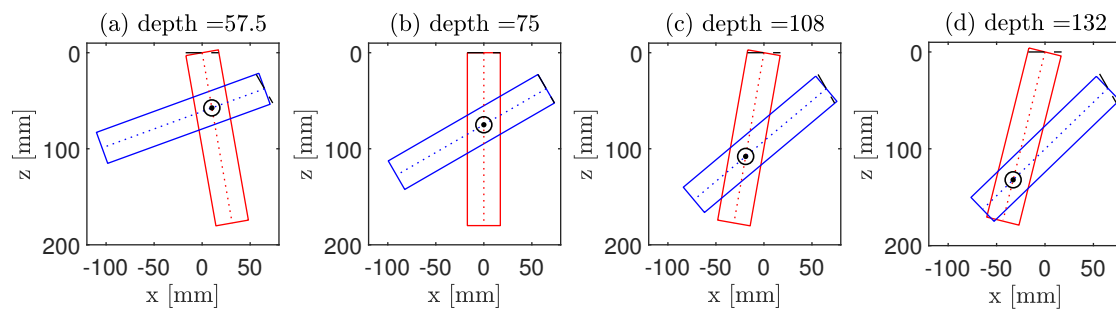


Figure 4. Schematic representation of the spatial location of the two linear arrays, T1 (red) and T2 (blue), and their FOV at different imaging depths. The circle indicates the centre of the common FOV, which defines the imaging depth in CoMTUS. Four different imaging depths are shown: (a) 57.5 mm; (b) 75 mm; (c) 108 mm; and (d) 132 mm.

3.1.3. CoMTUS through Layered Media

To investigate the effect of layers with different speeds of sound in the medium, three different kinds of tissue were defined in the propagation media (general soft tissue, fat and muscle). The imaging depth was set to 75 mm with a configuration of the arrays in space that defines an effective aperture of 104.7 mm with a 45.3 mm gap. The acoustic properties assigned to each tissue type were chosen from the literature [27] and are listed in Table 1. A medium defined only with the soft tissue properties was used as the control case. Then, clutter effects were analysed by using heterogeneous media in which two layers with the acoustic properties of muscle and fat were introduced into the control case medium. In the different studied cases, the thickness of the muscle layer was set to 8 mm while fat ranged from 5 to 35 mm in thickness. Figure 2 shows an example of the propagation medium with a muscle layer of 8 mm in thickness and a fat layer of 25 mm.

Aberration parameters were estimated using a one-dimensional version of the reference waveform method [28]. In these measurements, a source located at the centre of the shared FOV of both arrays that emits a spherical wave pulse that propagates through the different tissue layers and is received by the CoMTUS effective aperture (i.e., the two linear arrays) was simulated. Then, the arrival time fluctuations (ATF) across the receiving effective aperture caused by each layered medium were calculated by subtracting a linear fit from these calculated arrival times. Energy level fluctuations (ELF) in the data were calculated by summing the squared amplitudes of each waveform over a 1.5 ms window, which isolated the main pulse, converting to decibel units, and subtracting the best linear fit from the resulting values. More details of these measurements can be found in [29].

3.2. In Vitro Experiments

A sequence similar to the one used in simulations was used to image a phantom. The imaging system consisted of two 256 channel Ultrasound Advanced Open Platform (ULA-OP 256) systems (MSD Lab, University of Florence, Florence, Italy) [30,31]. The systems were synchronized, i.e., with the same trigger and sampling times in both transmit and receive mode. Each ULA-OP 256 system was used to drive an ultrasonic linear array made of 144 piezoelectric elements with a 6 dB bandwidth ranging from 2 MHz to 7.5 MHz (imaging transducer LA332, Esaote, Florence, Italy). The two probes were mounted on an xyz translation and rotation stage (Thorlabs, Newton, NJ, USA) and were carefully aligned in the same elevational plane ($y = 0$). For each probe in an alternating sequence, i.e., only one probe transmits at each time while both probes receive, seven PWs, covering a total sector angle of 30° (from -15° to 15° , 5° step), were transmitted at 3 MHz and pulse repetition frequency (PRF) of 1 kHz. RF data backscattered up to 135 mm deep were acquired at a sampling frequency of 19.5 MHz. No apodization was applied either on transmission or reception.

A subset of the simulated results was experimentally validated in vitro. A phantom custom made as described in [10], with three point-like targets and an anechoic region, was imaged with the

imaging system and pulse sequences described above. The average SOS of the phantom was 1450 m/s. The phantom was immersed in a water tank to guarantee good acoustic coupling. To model a layered medium with changes in SOS, a layer of paraffin wax of 20 mm in thickness was placed between the probes and the phantom. The measured SOS of the paraffin wax was 1300 m/s. The control experiment was performed first without the paraffin wax sample present. After the control scan, the paraffin wax sample was positioned over the phantom without the movement of the phantom or tank. Then, the target was scanned as before. The paraffin wax sample was positioned to sit immediately over the phantom, coupled to the transducers by water. A final control scan was performed to verify the registration of the phantom, tank and transducers, after the paraffin wax sample was scanned and removed.

3.3. Data Processing

The RF data, both simulated and experimentally acquired, were processed in different combinations to study image quality. The multi-transducer beamforming was performed as described in Section 2, Equations (1)–(3), and the optimum beamforming parameters, calculated as described in Section 2 (Equation (5)), were used to generate CoMTUS images. For the simulated RF data, where the actual position of the arrays in space is known, an additional image, noted as 2 probes, was beamformed by assuming an SOS of 1540 m/s and using the spatial location of the array elements. Note that, in the experimental case, this is not possible because the actual position of the arrays in space is not accurately known. Finally, the data corresponding to the sequence when the array T1 transmits and receives, i.e., T_1R_1 , and noted here as one probe, was used as a baseline for array performance, providing a point of comparison to the current coherent PW compounding method [15] in both simulated and experimental scenarios. Note that, for all the cases except CoMTUS, an assumed value of the SOS was used to beamform the data (1540 m/s for simulated data and 1450 m/s for experimental data).

In order to achieve a comparison between imaging modalities that is as fair as possible in terms of transmitted energy, the CoMTUS and the 2 probes images are obtained by compounding only six different PWs, while the one probe system images are generated compounding the total number of the transmit PWs, i.e., seven PWs from -15° to 15° , in 5° steps. Specifically for the CoMTUS and 2 probe images, the results use compounded RF data when the array T1 transmits PW at zero and positive angles ($0^\circ, 5^\circ, 10^\circ$) and the array T2 transmits PW at zero and negative angles ($0^\circ, -5^\circ, -10^\circ$). An even number of transmissions was set because the CoMTUS optimization is based on pairs of transmissions, one per array (Equation (6)). In addition, firing at opposite angles with the two arrays guarantees the CoMTUS performance since an overlap of the isonated regions is mandatory to determine the relative probe-to-probe position [10].

For each resulting image, lateral resolution (LR), contrast and the contrast-to-noise ratio (CNR) were measured to quantify the impact of both the aperture size and the clutter. LR was calculated from the point-spread-function (PSF) of the middle point target. An axial-lateral plane for 2D PSF analysis was chosen by finding the location of the peak value in the elevation dimension from the envelope-detected data. Lateral and axial PSF profiles were taken from the centre of the point target and aligned with the principal resolution directions. LR was then assessed by measuring the width of the PSF at the -6 dB level. The contrast and CNR were measured from the envelope-detected images [32]. Contrast and CNR were calculated as: $\text{Contrast} = 20 \log_{10}(\mu_i/\mu_o)$ and $\text{CNR} = |\mu_i - \mu_o| / \sqrt{\mu_i^2 + \mu_o^2}$, where μ_i and μ_o are the means of the signal inside and outside of the region, respectively, and at the same imaging depth. A circular region of 10 mm in diameter was used for these calculations.

4. Results

4.1. Simulation Results

4.1.1. Control Case: Conventional Aperture Imaging

The conventional aperture image, corresponding to the sequence when the array T1 transmits and receives (one probe) provides the baseline for imaging quality through the different scenarios. Figure 5a,f illustrates the resulting point target and lesion images at a 75 mm depth and without any aberrating layer in the propagation medium. An SOS of 1540 m/s was used to reconstruct these images. The point target (Figure 5a) has an LR of 1.78 mm, and the lesion (Figure 5f) is visible with a contrast of -16.78 dB and CNR of 0.846. Note that, while the lesion is easily identified from the background, it is difficult to delineate its edges.

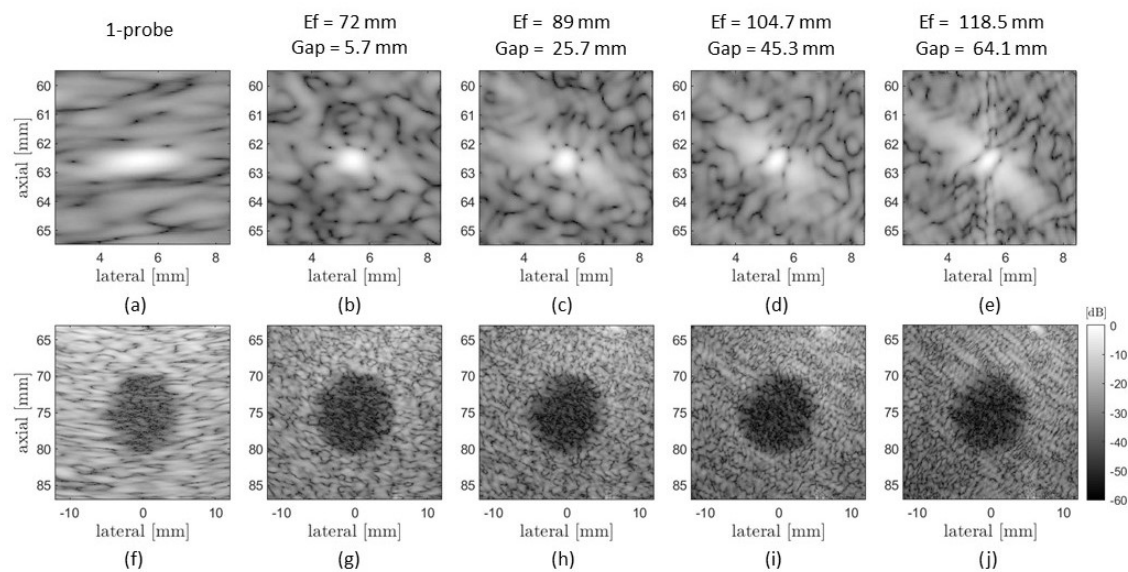


Figure 5. Simulated point targets (upper row) and lesion images (lower row) of the control medium obtained by one probe (a,f) and CoMTUS (b–e,g–j) with different effective apertures (E_f) and gaps between the two arrays (Gap).

4.1.2. CoMTUS Discontinuous Effective Aperture

Figure 5 shows the simulated PSF and lesion images from the same non-aberrating medium and for increasing the effective aperture and gap of the CoMTUS system. The control case (one probe) is used for comparison (Figure 5a,f). It can be seen that the PSF depends on the size of the effective aperture and the gap between the arrays, and its shape is dictated by the position of the arrays. A similar shape can be observed in the speckle of the lesion images (Figure 5g–j), where the texture shows the same trend as the point target images (Figure 5b–e). Note that a more conventional PSF shape, where the best spatial resolution is aligned with the x-axis, could be obtained by defining the global coordinate system of CoMTUS images at the centre of the effective aperture created by the two arrays [10]. The corresponding lateral PSFs extracted from the point target images are shown in Figure 5a, where it is possible to quantify the width of the main lobe and the amplitude of the side lobes. As expected, the central lobe of the PSF reduces in width with the increase in size of the effective aperture, and so does the speckle size. However, while at extended apertures, the width of the main lobe decreases, the amplitude of the side lobes increases with the corresponding gap in the aperture, affecting the contrast, as can be seen in the lesion images (Figure 5g–j).

The corresponding computed image quality metrics (LR, contrast and CNR) as a function of the obtained effective aperture are compared with the one probe system in Figure 6. Results show that both the main lobe of the PSF and the LR decrease with a larger effective aperture size. Since an increasing effective aperture represents also a larger gap between the probes, contrast and resolution follow opposite trends. In general, comparing with the one probe system, CoMTUS produces the best lateral resolution in all the cases, but shows degradation in contrast with increasing probe separation. At the minimum separation, CoMTUS produces an improvement in resolution compared to one probe of more than 50% (0.70 mm vs. 1.78 mm) combined with an improvement in contrast and CNR (−17.23 dB vs. −16.78 dB and 0.854 vs. 0.846, respectively). At the maximum effective aperture simulated, resolution is the best with 0.34 mm, while the contrast and CNR drop to a minimum of −15.51 dB and 0.82, respectively.

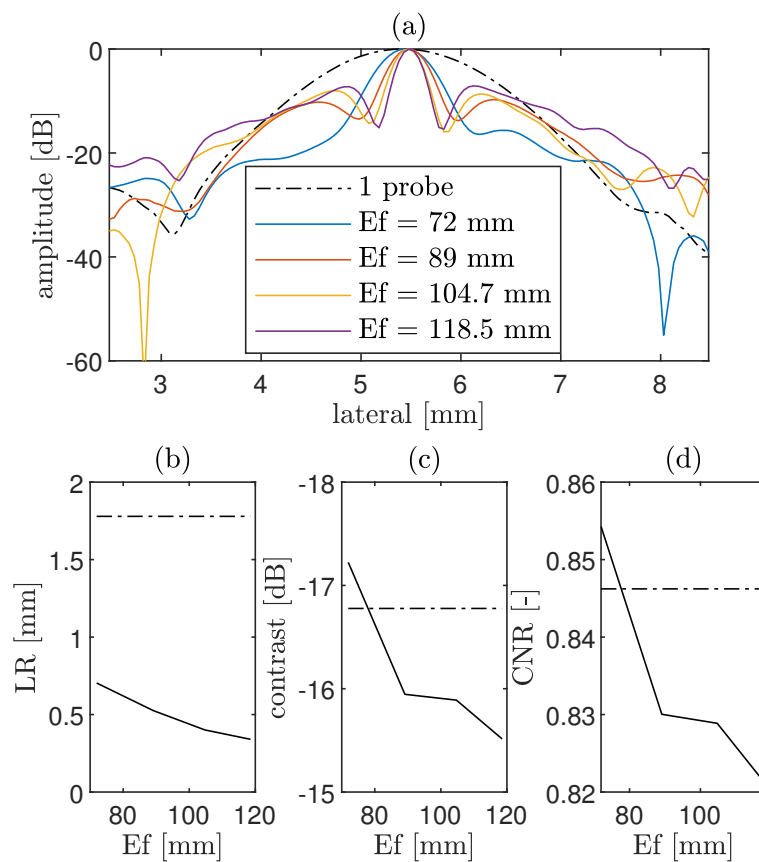


Figure 6. (a) Lateral point-spread-function (PSF) extracted from Figure 5 at the depth of peak point intensity and in the principal direction. Corresponding computed quality metrics as a function of the effective aperture size in CoMTUS (solid line) compared with the one probe system (dashed line): (b) lateral resolution (LR); (c) contrast; and (d) contrast-to-noise-ratio (CNR).

4.1.3. CoMTUS Imaging Depth

Figure 7 compares the one probe with the CoMTUS (gap ~45.3 mm) images at two different imaging depths (100 mm and 155 mm). Image degradation with depth is clearly observed in all the cases. However, at larger depths, the one probe shows a greater level of degradation. At the maximum imaging depth shown (155 mm), the point targets and the lesion can still be clearly identified in the CoMTUS image while they are barely discernible in the one probe image.

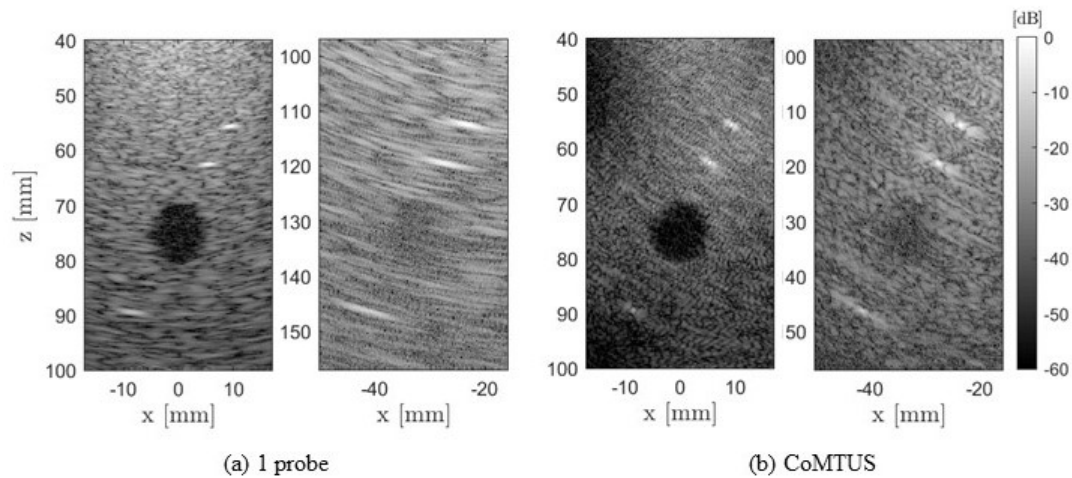


Figure 7. Comparison of simulated images of the non-aberrating medium at different imaging depths acquired by (a) one probe and (b) CoMTUS.

The computed image metrics as a function of the imaging depth are summarized in Figure 8. As expected, in both systems, all image metrics worsen at larger imaging depths. Nevertheless, results show that their dependence on the imaging depth is different. LR is always larger (worse) with one probe and increases more rapidly with depth (Figure 8a). While at reduced imaging depths (<100 mm), contrast and CNR seem to be affected in a similar way in both systems, the loss in contrast metrics is less accentuated in the CoMTUS system at depths larger than 100 mm. In those cases, the CoMTUS method exceeds the performance of the one probe system not only in terms of resolution, but also in contrast, despite in the used configuration, the gap in the aperture is not minimum and leads to greater side lobes (Figure 5d). The extended effective aperture created by CoMTUS consequently increases the sensitivity of the imaging system, particularly at large imaging depths.

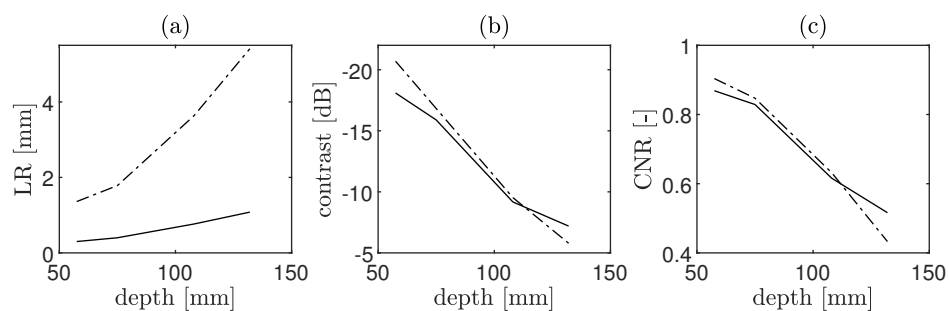


Figure 8. Computed quality metrics as a function of the imaging depth: (a) lateral resolution (LR); (b) contrast; and (c) contrast-to-noise-ratio (CNR). Two different methods are compared: one probe (dashed line) and CoMTUS (solid line).

4.1.4. CoMTUS through Layered Media

Aberration parameters measured from the simulated data are listed in Table 2. ATF and ELF are defined relative to the arrival time and energy profiles expected for an undistorted spherical wavefront. Comparing with the range of rms ATF values from previous studies [33], the aberrating strength introduced by the layered model can be considered from “weak” to “moderate”. Received wavefronts after geometric compensation are shown in Figure 9. Shape distortions, resulting from the propagation of the wavefront through the tissue layers, are apparent in the receiving aperture in all cases.

Table 2. Aberration parameters. Root-mean-squared (rms) values and full-width at half-maximum correlation lengths (CL) of arrival time and energy level fluctuations (ATF and ELF, respectively).

Fat + Muscle Thickness (mm)	rms ATF (ns)	ATF CL (mm)	rms ELF (dB)	ELF CL (mm)
5 + 8	0.94	0.35	2.48	4.86
10 + 8	13.74	8.17	2.49	4.84
15 + 8	22.09	9.75	2.48	4.84
20 + 8	23.03	8.76	2.47	4.82
25 + 8	32.53	9.34	2.47	4.80
30 + 8	35.64	7.44	2.48	4.80
35 + 8	39.64	9.37	2.49	4.75

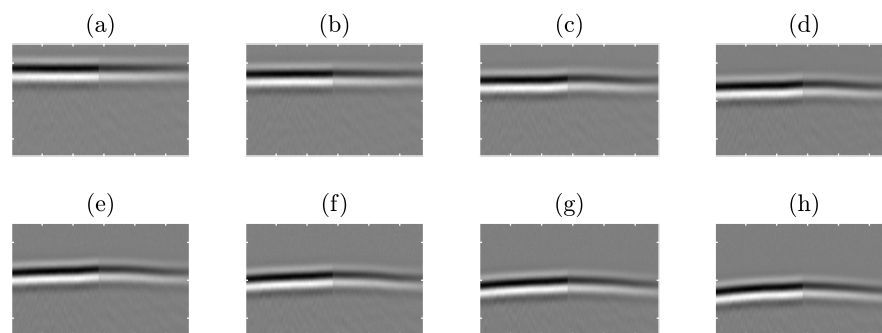
**Figure 9.** Simulated received wavefronts by the effective aperture after geometric compensation. Wavefronts are shown on a linear grey scale with time as the vertical axis and element number as the horizontal axis. The temporal range shown is 2.92 ms for 288 elements. Cases with different thicknesses of fat layer are shown: (a) 0 mm (control case); (b) 5 mm; (c) 10 mm; (d) 15 mm; (e) 20 mm; (f) 25 mm; (g) 30 mm; (h) 35 mm.

Figure 10 shows the simulated images for the control case (medium only with soft tissue) and for imaging through fat and muscle layers of 35 mm and 8 mm in thickness, respectively. The different methods (i.e., one probe, two probes coherently combined assuming probe locations are known and the SOS is constant and fully optimized CoMTUS) are compared. It can be seen that in the presence of aberration, the PSF and contrast of the 2 probes image significantly degrade when comparing with the control case. Indeed, in the presence of aberration, it is not possible to coherently reconstruct the image using the two separate transducers with fixed parameters (Figure 10e). However, the CoMTUS system retains its performance (Figure 10f).

Figure 11 shows an example of the delayed echoes from the point-like target for the 2 probes and CoMTUS cases, corresponding to a propagation medium with a fat layer of 35 mm in thickness. These flat echoes are obtained by coherently adding the four delayed backscattered echoes from the same point-like target ($T_1R_1, T_1R_2, T_2R_1, T_2R_2$) using Equation (3) and the corresponding beamforming parameters. In the 2 probes case, the different echoes do not properly align, creating interference when forming a coherent addition of signals. However, after optimizing the beamforming parameters in CoMTUS, all echoes substantially align and can be coherently added together, minimizing the aberrating consequences. Similar effects are seen in the anechoic lesion. While differences in the background speckle pattern are observed between the different imaging methods, a higher loss of contrast due to aberration can be appreciated only in the 2 probes images. No significant changes in image quality resulting from aberration are appreciated in either the one probe or CoMTUS systems. Although both systems are able to image through aberrating layers, they show clear differences. CoMTUS shows more detailed images than the one probe system. The speckle size is reduced, and the different tissue layers are only visible in the CoMTUS images.

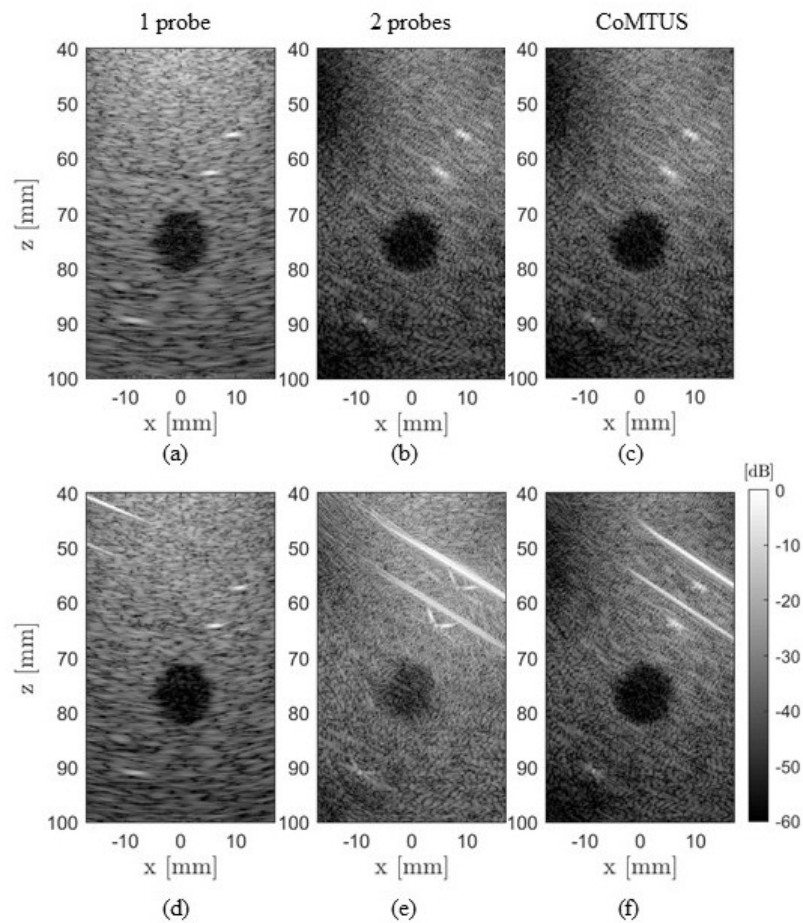


Figure 10. Comparison of simulated images for the control case (a–c) and imaging through fat and muscle layers of 35 mm and 8 mm in thickness, respectively (d–f). Different methods are compared: one probe, 2 probes and CoMTUS.

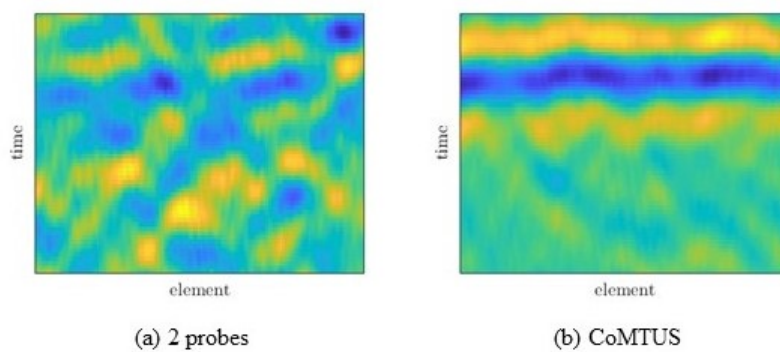


Figure 11. Simulated delayed RF data for a medium with a fat layer of 35 mm in thickness and backscattered from a point-like target, obtained by coherently adding the four delayed backscattered echoes from the same point-like target ($T_1R_1, T_1R_2, T_2R_1, T_2R_2$) using different beamforming parameters: (a) 2 probes; (b) CoMTUS.

The corresponding imaging metrics as a function of fat layer thickness are shown in Figure 12. As expected, in the absence of aberration, resolution improves with increasing aperture size. In this case, the worst lateral resolution corresponds to the one probe system with 1.78 mm, which is the one with the smallest aperture size, while the 2 probes and CoMTUS images are similar with 0.40

mm. The trends show that if aberration is not corrected, there are no significant improvements in the imaging metrics related to the aperture size for thicker fat layers. At a clutter thickness greater than 10 mm, image quality of the system formed by two transducers without aberration correction (2 probes) is significantly degraded, while CoMTUS imaging metrics are not affected by aberration errors, following the same trend as a conventional aperture (one probe) and providing a constant value of resolution over clutter thickness without any significant loss of contrast. At the thickest fat layer simulated, resolution is 1.7 mm and 0.35 mm for the one probe and CoMTUS images, respectively, while in the case of 2 probes images, it is no longer possible to reconstruct point-targets with sufficient definition to measure resolution. Contrast and CNR also show a similar significant loss for the 2 probes images. With the thickest aberrating layer, the 2 probes case gives a contrast of -10.84 dB and a CNR of 0.69, while those values are significantly better for the one probe (-18.44 dB contrast and 0.87 CNR) and CoMTUS (-17.41 dB contrast and 0.86 CNR) images.

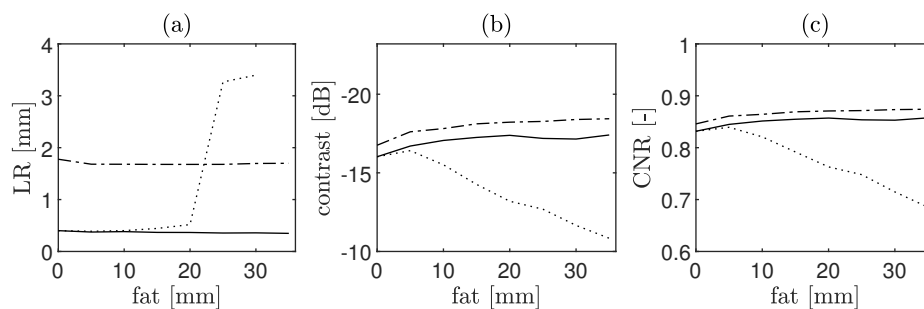


Figure 12. Computed quality metrics: (a) lateral resolution (LR), (b) contrast and (c) contrast-to-noise-ratio (CNR), as a function of the clutter thickness (fat layer). Three different methods are compared: one probe (solid line), 2 probes (dot line) and CoMTUS (dashed line).

4.2. Experimental Results

Coherent PW imaging with a conventional aperture (using a single probe) provides the reference for image quality with and without the paraffin wax layer.

To reconstruct these images, the reference SOS in water of 1496 m/s was used, and seven PWs were compounded. Figure 13 shows a comparison of the phantom images acquired with one probe and CoMTUS in the control case and through the paraffin wax sample. The CoMTUS images were reconstructed using the adaptively optimised beamforming parameters, which include the average SOS and compounding six PWs. All images are shown in the same dynamic range of -60 dB. In both cases, one probe and CoMTUS images, little variation is observed between the control and the paraffin images, which is consistent with the simulation results. The values of the optimum beamforming parameters used to reconstruct the CoMTUS images are $\{c = 1488.5 \text{ m/s}, \theta_2 = 30.04^\circ, \mathbf{r}_2 = [46.60, 12.33] \text{ mm}\}$ for the control case and $\{c = 1482.6 \text{ m/s}, \theta_2 = 30.00^\circ, \mathbf{r}_2 = [46.70, 12.37] \text{ mm}\}$ for the paraffin. There are slight changes in all the values and a drop in the average SOS, which agrees with the lower SOS of the paraffin wax. Figure 14 summarizes the computed image metrics for both the control and the paraffin cases. Little variation was observed in all the imaging metrics. Although minimum image degradation by aberrating layers was observed in CoMTUS, the overall image quality (particularly resolution) improved compared with the conventional single aperture, and the observed image degradation follows the same trend.

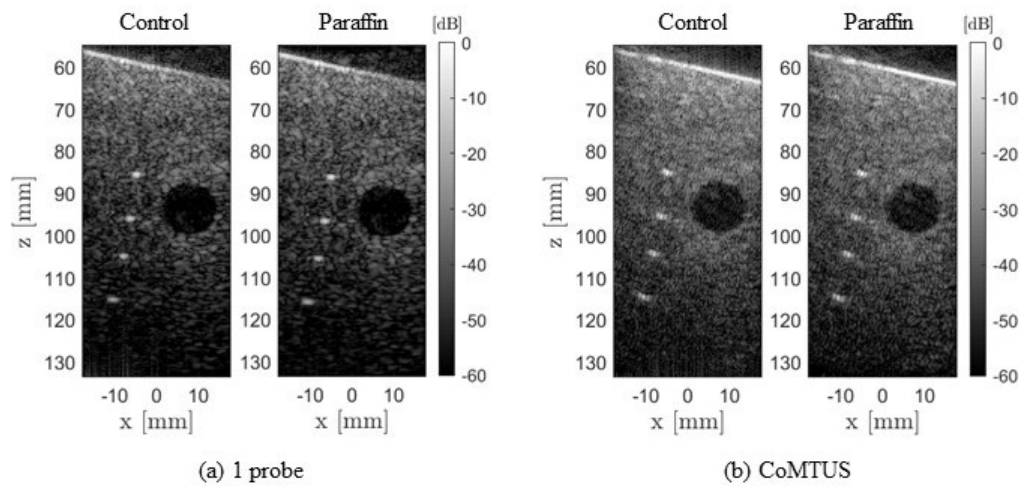


Figure 13. Experimental images of the control and the paraffin cases. Two different methods are compared: (a) one probe; and (b) CoMTUS.

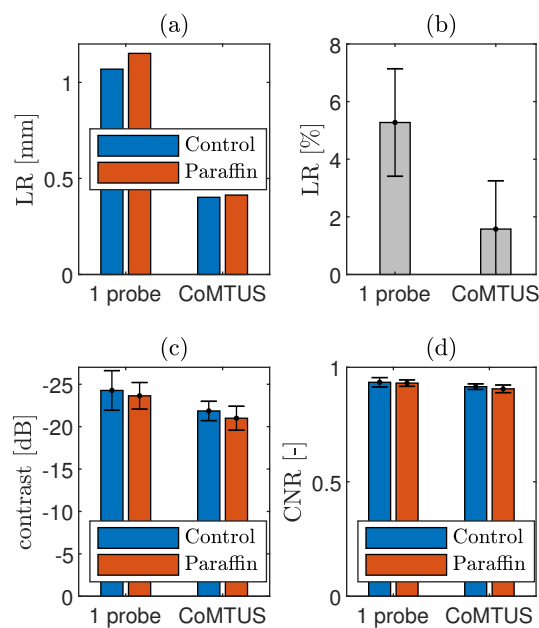


Figure 14. Computed quality metrics experimentally measured. (a) Lateral resolution (LR) measured at an 85 mm depth; (b) changes in LR measured in the four point targets when imaging through the paraffin and relative to the control case; (c) contrast; and (d) contrast-to-noise-ratio (CNR). Two different methods are compared: one probe and CoMTUS.

The first point target located at an 85 mm depth was described using its lateral PSF (Figure 15), with and without the paraffin wax layer. No significant effects due to aberration are observed in the PSF in any of the cases. The PSF shape is similar with and without the paraffin wax layer and agrees with the one observed in simulations. In general, the CoMTUS method leads to a PSF with a significantly narrower main lobe, but also with side lobes of bigger amplitude than the one probe conventional imaging system.

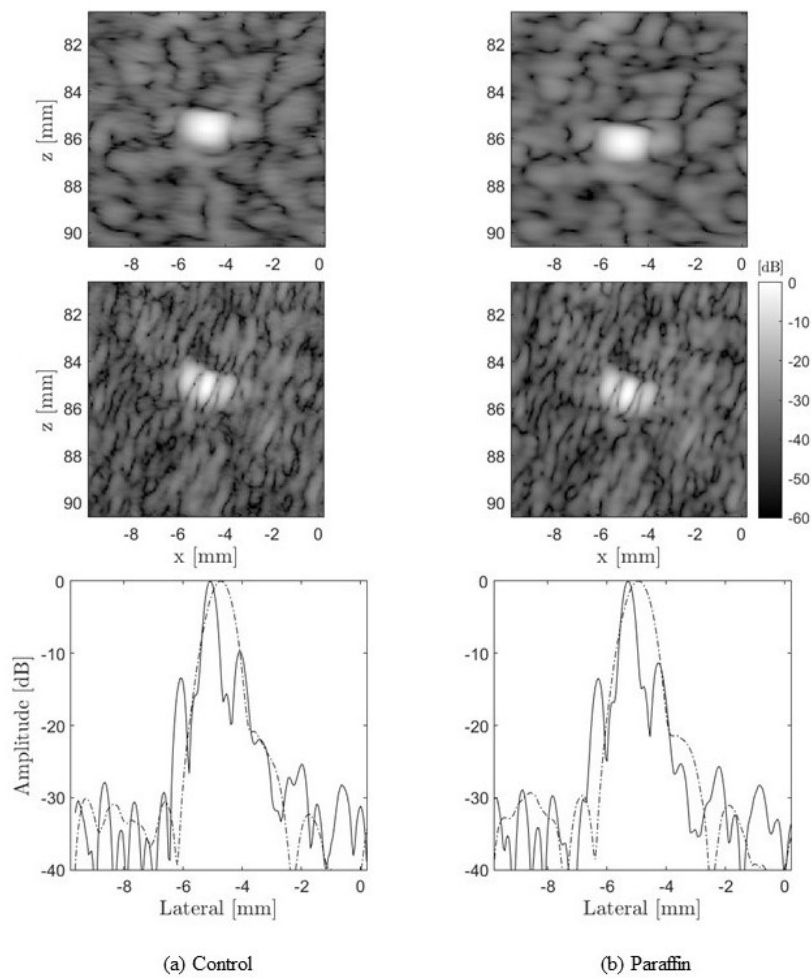


Figure 15. Experimental point target images. Column (a) corresponds to the control and column (b) to the paraffin. The first row corresponds to the one probe system and the middle row to CoMTUS. The bottom row shows the corresponding lateral point spread functions for the two cases displayed: one probe system (dashed line) and CoMTUS (solid line).

Figure 16 shows the coherent summation of the delayed echoes from the point-like target before and after optimization. The effects of the paraffin layer are clearly seen. When the beamforming parameters, including the averaged SOS, are optimized by the CoMTUS method, all echoes align better, minimizing the aberrating paraffin effects.

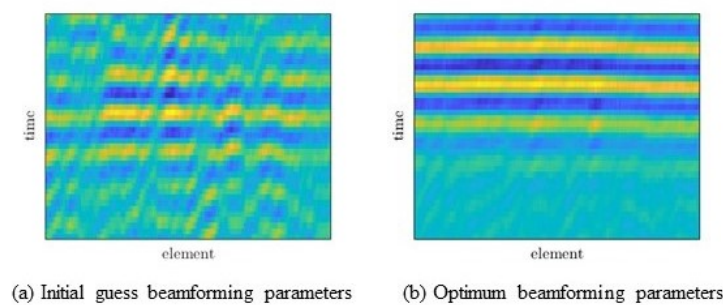


Figure 16. Experimental delayed RF data acquired from the phantom with the paraffin wax sample. CoMTUS flat backscattered echo from a point-like target, obtained by coherently adding the four delayed backscattered echoes from the same point-like target ($T_1 R_1, T_1 R_2, T_2 R_1, T_2 R_2$) using different beamforming parameters: (a) initial guess values; (b) optimum values.

5. Discussion

The implications for imaging using the CoMTUS method with two linear arrays are further investigated here with simulations and experiments. This analysis showed that the performance of CoMTUS depends on the relative location of the sub-arrays; the CoMTUS sensitivity increases with the imaging depth; and the resulting extended aperture is preserved in the layered media with different SOS. These findings show that, if the separation between the transducers is limited, the extended effective aperture created by CoMTUS confers benefits in resolution and contrast that improve image quality, particularly at large imaging depths, compared with a single probe standard system, and even in the presence of acoustic clutter imposed by tissue layers of different SOS (Figures 10 and 13). Extra analyses would be needed to quantify the significance of the results in different scenarios and further support these claims.

Unlike the improvement achieved in resolution, benefits in contrast are not so significant. Indeed, simulation results suggest that the discontinuous effective aperture may degrade contrast when the gap in the aperture is bigger than a few centimetres. In the probe design, there is a requirement of half wavelength spacing between elements in order to avoid the occurrence of unwanted grating lobes in the array response [34]. Moreover, previous studies indicated that, unlike resolution, contrast does not continue to increase uniformly at larger aperture sizes [7,35]. Nevertheless, while the contrast may be degraded by big discontinuities in the aperture, the main lobe resolution continues to improve at larger effective apertures. Since the lesion detectability is a function of both the contrast and resolution [36], overall, there are benefits from the extended aperture size, even when the contrast is limited. A narrow main lobe allows fine sampling of high resolution targets, providing improved visibility of the edges of clinically relevant targets. Both numerical and experimental results show how the speckle size significantly reduces when there is an enlarged receiving aperture produced by the coherent combination of multiple probes (Figures 5 and 15). In addition, when imaging at larger depths, an extended aperture has the potential to improve the attenuation limited image quality. In those challenging cases at large imaging depths, CoMTUS shows improvements not only in resolution, but also in contrast, even for effective apertures with significant gaps that raise the sidelobes (Figures 7 and 8).

Our results agree with the hypothesis that in the absence of aberration, the aperture size determines resolution [1]. However, previous works suggest that despite predicted gains in resolution, there are practical limitations to the gains made at larger aperture sizes [3]. Inhomogeneities caused changes in the sidelobes and focal distance, limiting the improvement in resolution. The resulting degradation is primarily due to the arrival time variation called phase aberration. The outer elements on a large transducer suffer from severe phase errors due to an aberrating layer of varying thickness, placing limits on the gains to be made from large arrays [37]. The findings presented here agree with these previous studies when there are fixed average parameters (coherent 2 probes case) in the presence of aberration clutter. However, the adaptive optimisation deployed in the CoMTUS method takes into account the average SOS along the propagation path in the medium and shows promise for extending the effective aperture beyond this conventional practical limit imposed by the clutter. More accurate SOS estimation improves beamforming and allows higher order phase aberration correction. However, other challenges imposed by aberration still remain. Recent studies reveal that both phase aberration and reverberation are primary contributors to degraded image quality [38]. While phase aberration effects are caused by variations in SOS due to tissue inhomogeneity, reverberation is caused by multiple reflections within an inhomogeneous medium, generating clutter that distorts the appearance of the wavefronts from the region of interest. For fundamental imaging, reverberations have been shown to be a significant cause of image quality degradation and are the principal reason why harmonic US imaging is better than fundamental imaging [39]. Since CoMTUS relies on detecting backscattered echoes from targeted scattered points, the optimization may be corrupted if the reverberation clutter overlays these echoes. The magnitude of this effect will depend mostly on the clutter strength and the signal-to-noise ratio. For all the cases described here, it was possible to detect the backscattered echoes

of the targets used for calibration, and CoMTUS optimization succeeded. However, there may be more complex situations in vivo, and further investigations are needed. Future work will focus on the role of redundancy in the large array in averaging multiple realizations of the reverberation signal as a mechanism for clutter reduction.

Finally, it should be acknowledged that some choices made in the design of this study may not directly translate to clinical practice, but we believe that they do not compromise the conclusions drawn from these results. The available experimental setup drove the election of the frequency at 3 MHz, which was higher than is traditionally used in abdominal imaging (1–2.5 MHz). However, the use of either lower or higher frequencies would have led to similar CoMTUS results, since the associated image benefits reported here are mainly dictated by the resulting extended effective aperture. In addition, both the simulated and experimental phantoms are a rather simplistic model of real human tissue. Simulations were limited to a two-dimensional model, while real ultrasound propagation occurs in three dimensions. In three dimensions, extra clutter can be generated also by off-axis scattering, arising from scatterers located away from the beam's axis. Second, although the tissue properties were taken from the literature, it is well known that ultrasonic tissue properties vary considerably among individual tissue specimens and different measurement techniques. Finally, the main limitation is the lack of tissue microstructure in the model. Only with a more complete description of tissue microstructure is it possible to capture the phase and amplitude errors observed in vivo in pulse echo measurements. However, the results presented here can capture the main time-shift fluctuations and then help in further understanding of CoMTUS. Previous simulation studies have shown that a simple model like the one used in this study successfully predicts the magnitudes and large-scale trends of time-shift fluctuations, but not the energy-level fluctuations and waveform distortions [29]. Further studies using more sophisticated models are needed to describe the wave distortions, including phase and energy fluctuations.

6. Conclusions

In this study, the implications for imaging using the CoMTUS method were further investigated by simulation and experiments. A CoMTUS system formed by two identical linear arrays was simulated using the k-wave Matlab toolbox to analyse the implications of different spatial parameters for imaging. A parametric study is presented, where the resulting effective aperture size, separation between the arrays, imaging depth and the presence of acoustic clutter were investigated. Results show that the performance of CoMTUS depends on the relative location of the arrays, that CoMTUS sensitivity increases with imaging depth and that the resulting extended aperture maintains its performance when imaging through a layered medium with different speed of sound. Both simulated and experimental results show that CoMTUS improves US imaging quality in terms of resolution and shows higher sensitivity with imaging depth, providing benefits to image quality compared with conventional one probe imaging systems.

7. Patents

L.P., R.J.E., and J.V.H. have the patent “Ultrasound method and apparatus”, GB-201810711-D0.

Author Contributions: Conceptualization, L.P.; methodology, L.P.; software, L.P. and A.R.; validation, L.P., A.R., and M.R.; formal analysis, L.P., A.R., R.J.E., and J.V.H.; investigation, L.P., A.R., M.R., R.J.E., and J.V.H.; resources, R.J.E. and J.V.H.; data curation, L.P. and M.R.; writing, original draft preparation, L.P.; writing, review and editing, L.P., A.R., M.R., R.J.E., and J.V.H.; visualization, L.P.; project administration, R.J.E. and J.V.H.; funding acquisition, J.V.H. All authors read and agreed to the published version of the manuscript.

Funding: This research was funded by the Wellcome Trust/EPSRC iFIND project, IEH Award (102431) (www.iFINDproject.com) and the Wellcome Trust/EPSRC funded Centre for Medical Engineering (WT 203148/Z/16/Z).

Acknowledgments: The authors acknowledge financial support from the Department of Health via the National Institute for Health Research (NIHR) comprehensive Biomedical Research Centre award to Guy's & St Thomas' NHS Foundation Trust in partnership with King's College London and Kings College Hospital NHS Foundation Trust.

Conflicts of Interest: The authors declare no conflict of interest.

References

1. Cobbold, R.S. *Foundations of Biomedical Ultrasound*; Oxford University Press: New York, NY, USA 2006.
2. Harris, R.A.; Follett, D.; Halliwell, M.; Wells, P. Ultimate limits in ultrasonic imaging resolution. *Ultrasound Med. Biol.* **1991**, *17*, 547–558. [[CrossRef](#)]
3. Moshfeghi, M.; Waag, R. In vivo and in vitro ultrasound beam distortion measurements of a large aperture and a conventional aperture focussed transducer. *Ultrasound Med. Biol.* **1988**, *14*, 415–428. [[CrossRef](#)]
4. Tsai, P.J.S.; Loichinger, M.; Zalud, I. Obesity and the challenges of ultrasound fetal abnormality diagnosis. *Best Pract. Res. Clin. Obstet. Gynaecol.* **2015**, *29*, 320–327. [[CrossRef](#)] [[PubMed](#)]
5. Klysiak, M.; Garg, S.; Pokharel, S.; Meier, J.; Patel, N.; Garg, K. Challenges of imaging for cancer in patients with diabetes and obesity. *Diabetes Technol. Ther.* **2014**, *16*, 266–274. [[CrossRef](#)] [[PubMed](#)]
6. Bottenus, N.; Long, W.; Zhang, H.K.; Jakovljevic, M.; Bradway, D.P.; Boctor, E.M.; Trahey, G.E. Feasibility of swept synthetic aperture ultrasound imaging. *IEEE Trans. Med. Imaging* **2016**, *35*, 1676–1685. [[CrossRef](#)] [[PubMed](#)]
7. Bottenus, N.; Long, W.; Morgan, M.; Trahey, G. Evaluation of Large-Aperture Imaging Through the ex Vivo Human Abdominal Wall. *Ultrasound Med. Biol.* **2018**, *44*, 687–701. [[CrossRef](#)] [[PubMed](#)]
8. Zimmer, V.A.; Gomez, A.; Noh, Y.; Toussaint, N.; Khanal, B.; Wright, R.; Peralta, L.; van Poppel, M.; Skelton, E.; Matthew, J.; et al. Multi-view Image Reconstruction: Application to Fetal Ultrasound Compounding. In *Data Driven Treatment Response Assessment and Preterm, Perinatal, and Paediatric Image Analysis*; Melbourne, A., Licandro, R., DiFranco, M., Rota, P., Gau, M., Kampel, M., Aughwane, R., Moeskops, P., Schwartz, E., Robinson, E., et al., Eds.; Springer International Publishing: Cham, Switzerland, 2018; pp. 107–116.
9. Peralta, L.; Gomez, A.; Hajnal, J.V.; Eckersley, R.J. Feasibility study of a coherent multi-transducer US imaging system. In Proceedings of the 2018 IEEE International Ultrasonics Symposium (IUS), Kobe, Japan, 22–25 October 2018; pp. 1–4.
10. Peralta, L.; Gomez, A.; Hajnal, J.V.; Luan, Y.; Kim, B.; Eckersley, R.J. Coherent Multi-Transducer Ultrasound Imaging. *IEEE Trans. Ultrason. Ferroelectr. Freq. Control* **2019**, *66*, 1316–1330. [[CrossRef](#)]
11. Peralta, L.; Gomez, A.; Hajnal, J.V.; Eckersley, R.J. Coherent multi-transducer ultrasound imaging in the presence of aberration. In Proceedings of the Medical Imaging 2019: Ultrasonic Imaging and Tomography, International Society for Optics and Photonics, San Diego, CA, USA, 17–18 February 2019; Volume 10955, p. 109550O.
12. Peralta, L.; Reinwald, M.; Hajnal, J.V.; Eckersley, R.J. Coherent Multi-Transducer Ultrasound Imaging through aberrating media. In Proceedings of the 2019 IEEE International Ultrasonics Symposium (IUS), Glasgow, UK, 6–9 October 2019; pp. 324–327.
13. Peralta, L.; Reinwald, M.; Ramalli, A.; Hajnal, J.V.; Eckersley, R.J. Extension of Coherent Multi-Transducer Ultrasound Imaging with Diverging Waves. In Proceedings of the 2019 IEEE International Ultrasonics Symposium (IUS) Glasgow, UK, 6–9 October 2019; pp. 2226–2229.
14. Fitzgibbon, A.W. Robust registration of 2D and 3D point sets. *Image Vis. Comput.* **2003**, *21*, 1145–1153. [[CrossRef](#)]
15. Montaldo, G.; Tanter, M.; Bercoff, J.; Benech, N.; Fink, M. Coherent plane-wave compounding for very high frame rate ultrasonography and transient elastography. *IEEE Trans. Ultrason. Ferroelectr. Freq. Control* **2009**, *56*, 489–506. [[CrossRef](#)]
16. Fang, B.T. Trilateration and extension to global positioning system navigation. *J. Guid. Control. Dyn.* **1986**, *9*, 715–717. [[CrossRef](#)]
17. Christensen-Jeffries, K.; Browning, R.J.; Tang, M.X.; Dunsby, C.; Eckersley, R.J. In vivo acoustic super-resolution and super-resolved velocity mapping using microbubbles. *IEEE Trans. Med. Imaging* **2014**, *34*, 433–440. [[CrossRef](#)] [[PubMed](#)]
18. Christensen-Jeffries, K.; Peralta, L.; Reinwald, M.; Hajnal, J.V.; Eckersley, R.J. Coherent Multi-Transducer Ultrasound Imaging with Micro-Bubble Contrast Agents. In Proceedings of the 2019 IEEE International Ultrasonics Symposium (IUS) Glasgow, UK, 6–9 October 2019; pp. 2310–2312.
19. Treeby, B.E.; Jaros, J.; Rendell, A.P.; Cox, B. Modeling nonlinear ultrasound propagation in heterogeneous media with power law absorption using a k-space pseudospectral method. *J. Acoust. Soc. Am.* **2012**, *131*, 4324–4336. [[CrossRef](#)]

20. Treeby, B.E.; Cox, B.T. k-Wave: MATLAB toolbox for the simulation and reconstruction of photoacoustic wave fields. *J. Biomed. Opt.* **2010**, *15*, 021314. [[CrossRef](#)] [[PubMed](#)]
21. Denarie, B.; Tangen, T.A.; Ekroll, I.K.; Rolim, N.; Torp, H.; Bjåstad, T.; Lovstakken, L. Coherent plane wave compounding for very high frame rate ultrasonography of rapidly moving targets. *IEEE Trans. Med. Imaging* **2013**, *32*, 1265–1276. [[CrossRef](#)] [[PubMed](#)]
22. Brown, J.; Christensen-Jeffries, K.; Harput, S.; Zhang, G.; Zhu, J.; Dunsby, C.; Tang, M.; Eckersley, R. Investigation of Microbubble Detection Methods for Super-resolution Imaging of Microvasculature. *IEEE Trans. Ultrason. Ferroelectr. Freq. Control* **2019**, [[CrossRef](#)]
23. Treeby, B.E.; Cox, B. Modeling power law absorption and dispersion for acoustic propagation using the fractional Laplacian. *J. Acoust. Soc. Am.* **2010**, *127*, 2741–2748. [[CrossRef](#)] [[PubMed](#)]
24. Pinton, G.F.; Dahl, J.; Rosenzweig, S.; Trahey, G.E. A heterogeneous nonlinear attenuating full-wave model of ultrasound. *IEEE Trans. Ultrason. Ferroelectr. Freq. Control* **2009**, *56*, 474–488. [[CrossRef](#)]
25. Robertson, J.L.; Cox, B.T.; Jaros, J.; Treeby, B.E. Accurate simulation of transcranial ultrasound propagation for ultrasonic neuromodulation and stimulation. *J. Acoust. Soc. Am.* **2017**, *141*, 1726–1738. [[CrossRef](#)]
26. Wise, E.S.; Robertson, J.L.; Cox, B.T.; Treeby, B.E. Staircase-free acoustic sources for grid-based models of wave propagation. In Proceedings of the 2017 IEEE International Ultrasonics Symposium (IUS), Washington, DC, USA, 6–9 September 2017; pp. 1–4.
27. Goss, S.; Johnston, R.; Dunn, F. Comprehensive compilation of empirical ultrasonic properties of mammalian tissues. *J. Acoust. Soc. Am.* **1978**, *64*, 423–457. [[CrossRef](#)]
28. Liu, D.L.; Waag, R.C. Correction of ultrasonic wavefront distortion using backpropagation and a reference waveform method for time-shift compensation. *J. Acoust. Soc. Am.* **1994**, *96*, 649–660. [[CrossRef](#)]
29. Mast, T.D.; Hinkelman, L.M.; Orr, M.J.; Sparrow, V.W.; Waag, R.C. Simulation of ultrasonic pulse propagation through the abdominal wall. *J. Acoust. Soc. Am.* **1997**, *102*, 1177–1190. [[CrossRef](#)] [[PubMed](#)]
30. Boni, E.; Bassi, L.; Dallai, A.; Guidi, F.; Meacci, V.; Ramalli, A.; Ricci, S.; Tortoli, P. ULA-OP 256: A 256-channel open scanner for development and real-time implementation of new ultrasound methods. *IEEE Trans. Ultrason. Ferroelectr. Freq. Control* **2016**, *63*, 1488–1495. [[CrossRef](#)] [[PubMed](#)]
31. Boni, E.; Bassi, L.; Dallai, A.; Meacci, V.; Ramalli, A.; Scaringella, M.; Guidi, F.; Ricci, S.; Tortoli, P. Architecture of an ultrasound system for continuous real-time high frame rate imaging. *IEEE Trans. Ultrason. Ferroelectr. Freq. Control* **2017**, *64*, 1276–1284. [[CrossRef](#)] [[PubMed](#)]
32. Smith, S.; Lopez, H.; Bodine, W., Jr. Frequency independent ultrasound contrast-detail analysis. *Ultrasound Med. Biol.* **1985**, *11*, 467–477. [[CrossRef](#)]
33. Laceyfield, J.C.; Pilkington, W.C.; Waag, R.C. Distributed aberrators for emulation of ultrasonic pulse distortion by abdominal wall. *Acoust. Res. Lett. Online* **2002**, *3*, 47–52. [[CrossRef](#)]
34. Lee, S.; Lo, Y. *Antenna Handbook: Theory, Applications, and Design*; Van Nostrand Reinhold: New York, NY, USA, 1988.
35. Bottenus, N.; Pinton, G.; Trahey, G. Large coherent apertures: Improvements in deep abdominal imaging and fundamental limits imposed by clutter. In Proceedings of the 2016 IEEE International Ultrasonics Symposium (IUS), Tours, France, 18–21 September 2016; pp. 1–4.
36. Karaman, M.; Li, P.C.; O'Donnell, M. Synthetic aperture imaging for small scale systems. *IEEE Trans. Ultrason. Ferroelectr. Freq. Control* **1995**, *42*, 429–442. [[CrossRef](#)]
37. Trahey, G.; Freiburger, P.; Nock, L.; Sullivan, D. In vivo measurements of ultrasonic beam distortion in the breast. *Ultrason. Imaging* **1991**, *13*, 71–90. [[CrossRef](#)]
38. Pinton, G.F.; Trahey, G.E.; Dahl, J.J. Spatial coherence in human tissue: Implications for imaging and measurement. *IEEE Trans. Ultrason. Ferroelectr. Freq. Control* **2014**, *61*, 1976–1987. [[CrossRef](#)]
39. Fatemi, A.; Berg, E.A.R.; Rodriguez-Molares, A. Studying the Origin of Reverberation Clutter in Echocardiography: In Vitro Experiments and In Vivo Demonstrations. *Ultrasound Med. Biol.* **2019**. [[CrossRef](#)]

Publisher's Note: MDPI stays neutral with regard to jurisdictional claims in published maps and institutional affiliations.



© 2020 by the authors. Licensee MDPI, Basel, Switzerland. This article is an open access article distributed under the terms and conditions of the Creative Commons Attribution (CC BY) license (<http://creativecommons.org/licenses/by/4.0/>).